Topology optimization of non-linear electromagnetic actuator based on Reluctance Network Analysis

Ming Yin, Nicolas Bracikowski, Mohammed Naidjate, Antoine Pierquin, Didier Trichet

To cite this version:

Ming Yin, Nicolas Bracikowski, Mohammed Naidjate, Antoine Pierquin, Didier Trichet. Topology optimization of non-linear electromagnetic actuator based on Reluctance Network Analysis. Journal of Magnetism and Magnetic Materials, 2024, 602, pp.172174. ⟨10.1016/j.jmmm.2024.172174⟩. ⟨hal-04650053⟩

HAL Id: hal-04650053
https://hal.science/hal-04650053v1

Submitted on 16 Jul 2024

Topology Optimization of Non-linear Electromagnetic Actuator based on Reluctance Network Analysis

Ming YIN [1], Mohammed NAIDJATE [2], Nicolas BRACIKOWSKI [1], Antoine PIERQUIN [1], Didier TRICHET [1]
[1]Institut de Recherche en Énergie Électrique de Nantes Atlantique, IREENA, UR 4642, Nantes Université,
F-44600 Saint-Nazaire, France, nicolas.bracikowski@univ-nantes.fr
[2] Polytechnique Montréal, Montréal, H3T 1J4, Canada, mohammed.naidjate@polymtl.ca

Topology Optimization (TO) enables unrestricted exploration within a design domain and is typically based on a spatial discretization that is also used as the mesh for simulation. In this article, we propose to use for the simulation a mesh-based equivalent circuit method termed the Reluctance Network Analysis (RNA), with nonlinear magnetic properties of the material. The simulation tool is then used in a topology optimization process solved with generalized optimality criteria (GOC) method. During the optimization, the sensitivity matrix is needed, and we describe here how to derive the matrix in the case of a nonlinear RNA using Adjoint Variable Method (AVM). Finally, we implemented this topology optimization through a case study of an electromagnetic actuator.

***Index Terms*—Topology optimization, electromagnetic actuator, reluctance network analysis, adjoint variable method.**

I. INTRODUCTION

TOPOLOGY OPTIMIZATION has received wide attention from electrical engineers since the seminal work by Bendsøe and Kikuchi [1]. Contrary to parametric optimization methods, topology optimization has no initial bias on the final topology. So, it may result in an entirely novel topology that cannot be imagined beforehand.

Topology optimization was first applied to electromagnetic fields by Dyck and Louther, who proposed the so-called optimized material distribution (OMD) method in [2]. And after, many other approaches have emerged, such as the ON/OFF method [3], topological derivative method [4], and level set method [5]. Among them, the density method is the most popular one illustrated by the large volume of applications of density-based representation in the area of electromagnetic design.

The general topology optimization problem is to find the material distribution in a design domain that minimizes an objective function f, subject to a volume V_0 or other constraints. An example of a discretized formulation of the optimization problem with a volume constraint (c) can be written as:

$$\begin{aligned} &\underset{\rho\in\mathbb{R}^{N_e}}{\arg\min} \quad f(\rho) \\ &\text{s.t.} \qquad c(\rho)=\sum_{e=1}^{N_e} v_e\rho_e - V_0 \leq 0 \end{aligned} \tag{1}$$

where N_e is the whole number of elements in the design domain, v_e is the element volume and ρ_e is the element material density within the range of [0,1].

To process topology optimization, a numerical model is required to characterize the performances and evaluate f. There are several approaches for modeling problems, and the two most commonly used are finite element analysis (FEA) and reluctance network analysis (RNA). FEA has been used since the 1990s to study magnetic transmission and is the main tool for accurate nonlinear simulations. The RNA is sometimes termed the magnetic equivalent circuit (MEC). There are two approaches for the RNA technique. The first approach features fewer elements with predefined flux paths to develop the magnetic circuit. The second approach is a mesh-based technique. In the latter technique, an electromagnetic device is discretized into elements first, then an equivalent circuit is associated with each element by defining the reluctances and magnetomotive force (MMF) sources [6]. The circuit is solved by the Kirchhoff circuit rules. By this method, the local saturation, mutual coupling, and leakage can be accounted. The accuracy and computation time of this technique is dependent on the device discretization level. In literature, different elementary geometries are applied, such as rectangular, triangular, full-part of cylinder, and hollow-part of cylinder [7], [8], [9]. Those different geometries also pave the way for application to topology optimization.

In the topology optimization of electromagnetic fields, a large volume of applications are based on FEA modeling. To the author's knowledge, there is still no topology optimization based on the RNA modeling.

We consider that RNA method has the advantage of simple implementation compare to FEM. The FEA tools require numerical methods knowledge and computational efforts do deal with weak formulation and integration. In comparison, the RNA model can be easily understood and applied by electrical engineer because it is only based on connectivity and circuit considerations. It is all the more interesting in the context of topological optimization because we need to modify assembling part. Finally, for similar mesh, accuracy and computation time are more or less comparable. Therefore, in topology optimization, the RNA as a non-FEA-based modeling framework has great potential and seems worth further exploring.

Electromagnetic actuators convert electrical energy to mechanical one. They are key machine components extensively applied in robotics, transportation, and manufacturing. Conventionally, parametric optimizations were conducted to maximize the magnetic attraction force with minimum power consumption [10]. In this study, we presented topological optimization to the electromagnetic actuator which is a classic benchmark in TO [11], [12], [13], [14] . This structure presented in Fig. 1 mainly consists of three parts as described in Fig. 1, the core (with a 'C' shape), the coil (in the yellow regions), and the armature (the moving part). Its operation principle is that when an electric current flows through the coil, it generates its own magnetic field. This field interacts with the magnetized armature, which leads to an attractive force between them. This work investigates a general framework of the 2D RNA method applied to topology optimization in the magnetostatic nonlinear case and opens up further exploration of this method. The article is organized as follows: First, the general framework of reluctance network modeling considering material saturation is discussed in section $II-A$. Next, the interpolation scheme, the determination of the objective function, and its sensitivity based on this model is depicted in section $II-B, C, D$. Then, the adopted optimization algorithm is discussed in section $II-E$. Finally, the results are discussed and analyzed in section III, IV.

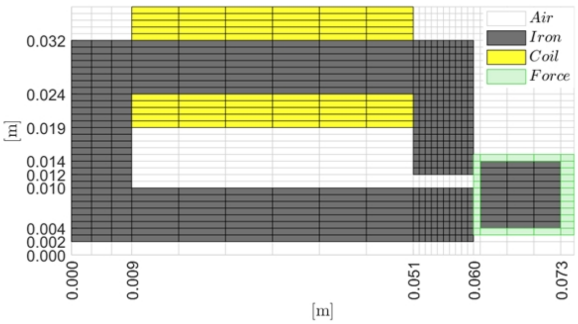

Fig. 1. The design of the electromagnetic actuator with the mesh

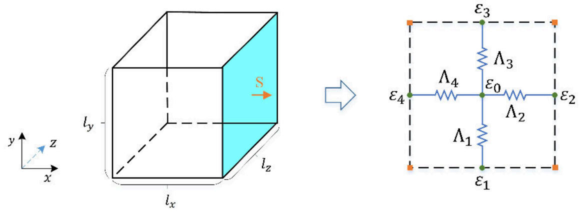

Fig. 2. The mesh element and its associated magnetic equivalent circuit

II. Problem definition

A. Reluctance Network Modeling

According to different material properties (ferromagnetic, copper, or air), the electromagnetic actuator is separated into several regions. Each of those regions can be further divided by layers, and the number of layers is a user-controlled parameter that determines the mesh discretization. Finally, the regions are decomposed into regular elements as illustrated in Fig. 1. It is noteworthy that in the RNA model, the mesh can be adjusted to provide a flexible solution, allowing for a fine mesh only in the relevant regions while maintaining a coarse mesh in others. This strategy can lead to acceptable accuracy with fewer unknowns. Then, we associate an elementary circuit, a 'cell', to each mesh element based on its physical characteristics. As illustrated in Fig. 2, there are two x-directed and two y-directed lumped reluctances connecting the center node to a cell boundary node. The value of reluctance can be determined based on element dimensions and the element permeability. Accordingly, the permeance (Λ) is expressed by the inverse of the lumped reluctance (R) which has the form (2)

$$\Lambda = \frac{1}{R} = \frac{\mu S}{l} \tag{2}$$

where S is the cell cross-section area normal to the flux path, taking into account the depth, l is the length of the flux path, and μ is the material magnetic permeability.

For the elements in the coil region, the magnetic field sources from the coil's current can be modeled by MMF source in series with reluctance located in the branch of x direction, as is illustrated by the equivalent circuit in Fig. 3(a). During the implementation phase, we can simplify the application of nodal analysis by transforming the equivalent circuit into the expression shown in Fig. 3(b) using Norton's theorem. The value of the flux source derives from:

$$\begin{aligned} \varphi_2^{coil} &= F_2^{coil}\Lambda_2 \\ \varphi_4^{coil} &= F_4^{coil}\Lambda_4 \end{aligned} \tag{3}$$

Fig. 4 depicts the variation of MMF in the coil region with the coordinate of the y-direction. To keep the same pattern of the equivalent circuit with Fig. 3 (b), the value of MMF sources outside the coil region can be assumed to be zero.

Apply Gauss's law for magnetism to the cell node and we get a node MMF equation of the form

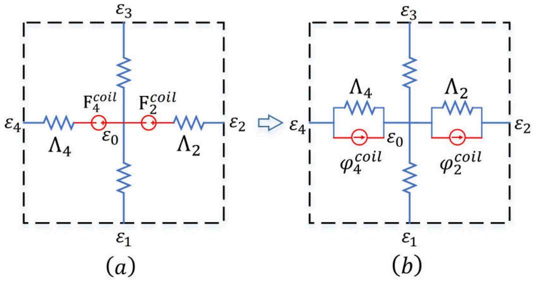

(a) (b)

Fig. 3. Magnetic equivalent circuit of the coil region

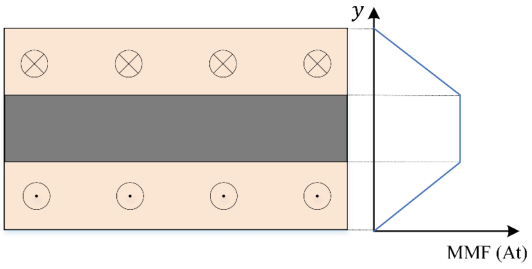

Fig. 4. The coil region and the variation of MMF

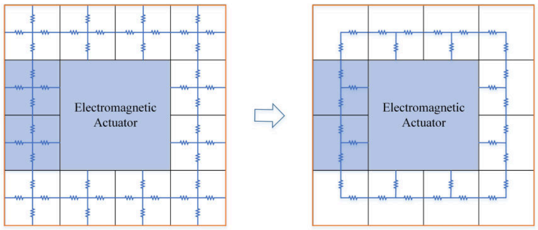

Fig. 5. Neumann boundary condition

$$\sum_{i=1}^{4}(\Lambda_i\varepsilon_0 - \Lambda_i\varepsilon_i) = -\varphi_2^{coil} + \varphi_4^{coil} \tag{4}$$

where ε is the node potential, and φ is the flux source due to excitation.

Each node in the reluctance network corresponds to a node MMF equation of the same form with (4). Collect those equations together, and express them in a matrix form:

$$[\Lambda]\{\varepsilon\} = \{\varphi\} \tag{5}$$

where $[\Lambda]$ is the system permeance matrix which is always symmetric and extremely sparse [6]. $\{\varepsilon\}$ is the column vector of unknown scalar magnetic potentials of each node, $\{\varphi\}$ is the column vector of the flux sources. Among the different boundary conditions [15], we imposed the Neumann condition to ensure that no flux leakage across the boundary of the study domain. This can be achieved by simply deleting reluctances normal to the boundary, as illustrated in Fig. 5.

Finally, solving the system of equations, and the scalar magnetic potentials are derived. Then, we can deduce other local quantities of interest, such as the flux density ($\vec{B}$), and global quantities, such as force ($\vec{F}$). The field distribution is localized at the centroid of each mesh element (e.g. e), and the two components of flux density in the Cartesian system are computed by (6).

$$\begin{aligned} B_x^e &= \frac{B_2^e + B_4^e}{2} = \frac{\Lambda_2^e(\varepsilon_0^e - \varepsilon_2^e) + \Lambda_4^e(\varepsilon_4^e - \varepsilon_0^e)}{2S_x^e} \\ B_y^e &= \frac{B_1^e + B_3^e}{2} = \frac{\Lambda_1^e(\varepsilon_1^e - \varepsilon_0^e) + \Lambda_3^e(\varepsilon_0^e - \varepsilon_3^e)}{2S_y^e} \end{aligned} \tag{6}$$

Where S_x^e, S_y^e is the cross-section surface normal to the x, and y direction separately. For regular mesh and the material property being linear (e.g. air), there is symmetry on both sides of the central node:

$$\begin{aligned} \Lambda_x^e &= \Lambda_2^e = \Lambda_4^e \\ \Lambda_y^e &= \Lambda_1^e = \Lambda_3^e \end{aligned} \tag{7}$$

Then, the formula(6) can be further simplified by (8):

$$\begin{aligned} B_x^e &= \frac{\Lambda_x^e}{2S_x^e}(\varepsilon_4^e - \varepsilon_2^e) \\ B_y^e &= \frac{\Lambda_y^e}{2S_y^e}(\varepsilon_1^e - \varepsilon_3^e) \end{aligned} \tag{8}$$

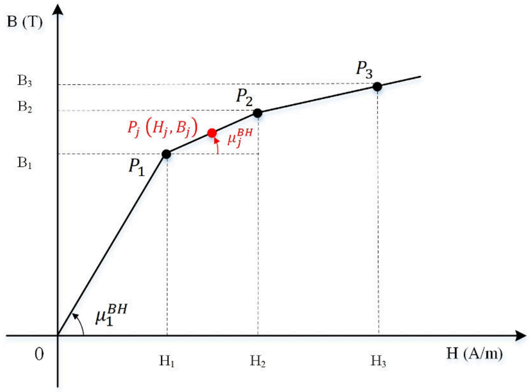

Fig. 6. B-H curve of nonlinear material

The material's behavior law is nonlinear if the material saturation effect is considered. It is typically solved by an iterative process, such as Newton's method or fixed point method [16]. In this work, we utilized the well-developed magnetic equivalent circuit model coupled with a single-valued B-H curve (SVC) described in [16], [17]. Along each branch in an element, we use a piecewise method to describe the B-H profile as depicted in Fig. 6. Then, their relation is represented using a piecewise function $B = f_{BH}(H)$, here, both B and H are scalars. Consider the condition where the working point (P_j) is located between two consecutive sampling points (P_n, P_{n+1}), and the B_j can be expressed as (9).

$$B_j = \underbrace{\frac{B_{n+1} - B_n}{H_{n+1} - H_n}}_{\mu_j^{BH}}(H_j - H_n) + B_n \tag{9}$$

Then, both sides of (9) are multiplied by the surface S. We obtain the equation (10).

$$B_j S = \frac{\mu_j^{BH} S}{l} H_j l + (B_n - \mu_j^{BH} H_n) S \tag{10}$$

It can be re-written in terms of the lumped circuit parameters:

$$\varphi_j = \Lambda_j^{BH} \Delta\varepsilon_j + \varphi_j^{BH} \tag{11}$$

where $\Delta\varepsilon_j$ is the magnetic potential drop due to H_j, Λ_j^{BH} and φ_j^{BH} are the Norton equivalent circuit values at the operating point P_j on the j slope. They have the following expressions:

$$\Delta\varepsilon_j = H_j l \tag{12}$$

$$\Lambda_j^{BH} = \frac{\mu_j^{BH} S}{l} = \frac{B_{n+1} - B_n}{H_{n+1} - H_n} \times \frac{S}{l} \tag{13}$$

$$\varphi_j^{BH} = (B_n - \mu_j^{BH} H_n) S = \frac{B_n H_{n+1} - B_{n+1} H_n}{H_{n+1} - H_n} \times S \tag{14}$$

$$\underbrace{\left([\Lambda^0] + [\Lambda_j^{BH}]\right)}_{[\Lambda(\{\varepsilon\})]}\{\varepsilon\} = \underbrace{\{\varphi^{coil}\} + \{\varphi_j^{BH}\}}_{\{\varphi(\{\varepsilon\})\}} \tag{15}$$

Then, the material saturation is modeled by introducing an additional flux source in parallel with a permeance and their

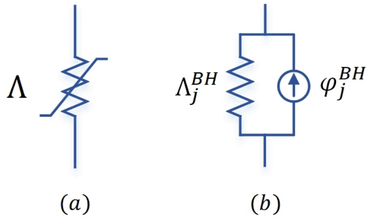

Fig. 7. (a) Nonlinear permeance and (b) its Norton equivalent circuit

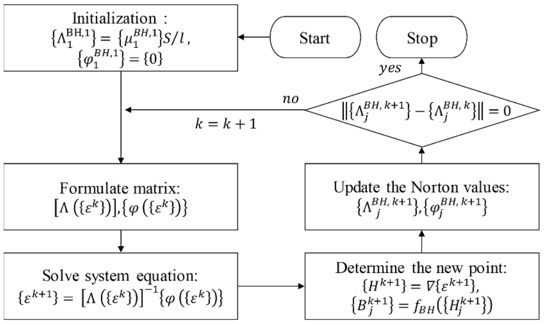

Fig. 8. The flowchart describing the iterative method developed for nonlinear material

values depend on the system solution $\{\varepsilon\}$, as shown in Fig. 7(b). Herein, the system equation (5) becomes nonlinear. We can decompose the permeance matrix $[\Lambda]$ and the source vector $\{\varphi\}$ into two terms, as indicated in (15): The first terms, $[\Lambda^0]$ and $\{\varphi^{coil}\}$, are related to linear material (air, coil) which are invariant with the system solution $\{\varepsilon\}$. The second terms, $[\Lambda_j^{BH}]$ and $\{\varphi_j^{BH}\}$, are related to the nonlinear material (iron), and they are updated by an iterative process. The updating algorithm is described in Fig. 8.

1) Initiate the iteration $(k = 1)$ and set the operating slope of all the nonlinear branches at the first one $(j = 1)$.
2) Formulate the system matrix $[\Lambda(\{\varepsilon^k\})]$ and flux source vector $\{\varphi(\{\varepsilon^k\})\}$.
3) Obtain the new node potentials $\{\varepsilon^{k+1}\}$ by solving the system equation.
4) Calculate the new field strength $\{H_j^{k+1}\}$ and flux density $\{B_j^{k+1}\}$ of nonlinear branches.
5) Update their Norton equivalent circuit values $\Lambda_j^{BH,k+1}$ and $\varphi_j^{BH,k+1}$ to the new operating point P_j^{k+1}.

Repeat from step 2) until all the operating slopes between two consecutive iterations are not changed, then the corresponding Norton equivalent circuits have the same values $(\|\{\Lambda_j^{BH,k+1}\} - \{\Lambda_j^{BH,k}\}\| = 0)$.

B. Material interpolation scheme

The element-wise volume fractions ρ, or material densities, that define topology are introduced as design variables. This continuous variable ranges $0 \leq \rho \leq 1$. $\rho = 1$ corresponds to a solid element and 0 to a void element. The other elements with $0 < \rho < 1$ are said to be the gray scale (virtual material, or intermediate material) which has no physical meaning. The representation of a domain Ω based on the material density is illustrated in Fig. 9. Concerning magnetic actuators, the physical properties of material such as magnetic permeability (μ) or magnetic reluctivity (ν) as in the article [13] are often interpolated with respect to the design variable ρ. There are many choices for the interpolation schemes, like the Rational Approximation of Material Properties (RAMP) proposed in [18] and the scheme proposed by D. Lukáš in [19]. A common approach is to adopt the modified Solid Isotropic Material with Penalization (SIMP) method [20]. The relationship between the density design variable and the material permeability is given by the power law (16):

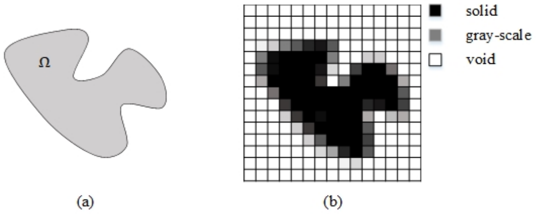

Fig. 9. (a) the reference domain Ω (b) and its density-based representation

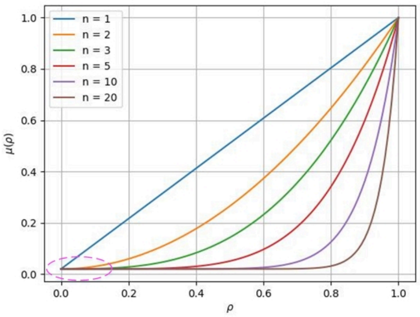

Fig. 10. The SIMP method and its numerical instability area

$$\mu_{virt}(\rho) = \mu_{air} + (\mu_{iron} - \mu_{air})\,\rho^n \tag{16}$$

where ρ is the density design variable, μ_{air} is the permeability of the air, and μ_{iron} is the permeability of the ferromagnetic material. The penalty coefficient, $n > 1$, has a certain regulation effect. The spread of material permeability μ is shown in Fig. 10 when different penalization factors are used.

Increasing n helps the optimization process to remove the 'gray-scale'. However, it is also accompanied by an increased risk of convergence problems. Sometimes, a minimal value ρ_{min} is required to prevent the difficulty of singularities of system matrices and zero sensitivity at zero density area [21]. Other new generalized interpolation schemes that prevent those issues mentioned can be found in [22].

For a fast solution, we introduced a simplified B-H curve with only two slopes. It has a knee point at B_{sat}, and the flux density exceeding this value would be saturated. Then, we can simply divide the operating point of nonlinear material into two conditions, linear and saturated. Also, the saturated material always has the same permeability as the air. The B-H is interpolated by the SIMP method continuously as depicted in Fig. 11. The different components of the nonlinear magnetic

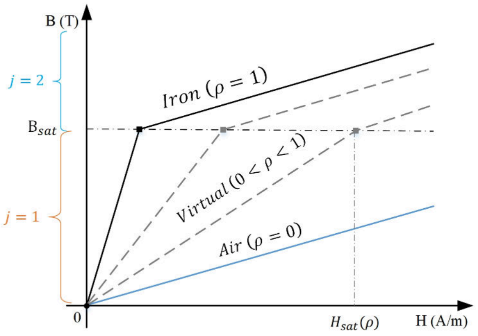

Fig. 11. The simplified B-H curves of material with interpolation

equivalent circuit in Fig. 6(b) can be identified by (17) and (19).

if $B < B_{sat}$,

$$\begin{cases} \Lambda^{j=1}_{virt}(\rho) = \rho^n \Lambda^{j=1}_{iron} + (1-\rho^n)\,\Lambda_{air} \\ \varphi^{j=1}_{virt} = 0 \end{cases} \tag{17}$$

(18)

else if $B \geq B_{sat}$,

$$\begin{cases} \Lambda^{j=2}_{virt} = \Lambda_{air} \\ \varphi^{j=2}_{virt}(\rho) = \varphi_{sat}\left(\dfrac{\Lambda^{j=1}_{virt}(\rho) - \Lambda_{air}}{\Lambda^{j=1}_{virt}(\rho)}\right) \end{cases} \tag{19}$$

where,

$$\begin{aligned} \Lambda^{j=1}_{iron} &= \frac{\mu_{iron} S}{l} \\ \Lambda_{air} &= \frac{\mu_{air} S}{l} \\ \varphi_{sat} &= B_{sat} S \end{aligned} \tag{20}$$

C. Magnetic Force computation

The optimization objective is to maximize the x-directional magnetic force (F_x) developed on the armature. According to the Maxwell Stress Tensor (MST) method [23], a surface enclosing the armature is chosen as the integration path, and the magnetic force ($\vec{F}$) is derived from the formula (21).

$$\vec{F} = \left[\oint \frac{1}{2\mu_0}(B_n^2 - B_t^2)ds\right]\vec{n} + \left[\oint \frac{1}{\mu_0} B_n B_t ds\right]\vec{t} \tag{21}$$

where $\vec{n}$ and $\vec{t}$ are unit vectors normal and tangential to the integration path. The different components of the magnetic flux density $\vec{B}$ can be deduced from the solution of (5) or (15).

The integration path is discretized by a set of elements (N^F_{cell}) enveloping the armature as indicated in Fig. 1. The mesh size of those elements can have an influence on the torque calculation accuracy. Usually, we keep fine mesh in the airgap close to the armature because the magnetic field varies greatly in this region. Rewrite (21) using branch permeances and magnetic potentials as described in (8), we get:

$$F_x = \sum_{e=1}^{N^F_{cell}} \frac{1}{4 l^e_x} \begin{Bmatrix} \Lambda^e_x(\varepsilon^e_4 - \varepsilon^e_2)^2 - \Lambda^e_y(\varepsilon^e_1 - \varepsilon^e_3)^2 \\ 2\Lambda^e_y(\varepsilon^e_4 - \varepsilon^e_2)(\varepsilon^e_1 - \varepsilon^e_3) \end{Bmatrix} \cdot \begin{Bmatrix} n^e_x \\ n^e_y \end{Bmatrix} \tag{22}$$

Where l_x is the element length, which varies with elements. n_x, n_y have a value of either 0 or 1, and they form a unit vector normal to the integration surface.

D. Sensitivity computation

The optimization involves both stochastic and deterministic methods. While the stochastic approach allows for global exploration, it comes with high computational costs. On the other hand, the deterministic method is more efficient but tends to converge to local optimal and requires sensitivity of the objective function. Sensitivity is very useful information for topology optimization to determine how changes in the design variables affect the objective function. There are mainly two kinds of sensitivity calculation methods in the literature,

- The Finite Difference Method (FDM)
- The Adjoint Variable Method (AVM)

The main finite difference methods used are the Forward Difference, Backward Difference, and Central Difference methods. The primary drawback of this method is that achieving all the requisite sensitivity of the objective function necessitates the number of simulations equivalent to the number of variables which is a time-intensive process. In comparison, the AVM requires only one additional simulation and is more efficient. However, the calculation of the gradient can sometimes be tedious or even impossible. The detailed derivation of this method is discussed in [24].

The formulation of the optimization problem can be expressed as:

$$\begin{aligned} \min \quad & -F_x(\{\varepsilon\}, \{\rho_e\}) \\ \text{s.t.} \quad & c(\{\rho_e\}) = \sum_{e=1}^{N_e} v_e \rho_e - V_0 \leq 0 \\ & \{g\} = [\Lambda(\{\varepsilon\}, \{\rho_e\})] \cdot \{\varepsilon\} - \{\varphi(\{\rho_e\})\} = \{0\} \\ & \rho_{min} \leq \rho_e \leq 1 \end{aligned} \tag{23}$$

The magnetic force F_x is an explicit function of the design variables $\{\rho_e\}$ and the intermediate variables $\{\varepsilon\}$. According to the chain rule, the derivative of the magnetic force F_x with respect to a design variable ρ_e (density ρ of element e) is written as (24).

$$\frac{dF_x}{d\rho_e} = \frac{\partial F_x}{\partial \rho_e} + \left(\frac{\partial F_x}{\partial\{\varepsilon\}}\right)^T \frac{d\{\varepsilon\}}{d\rho_e} \tag{24}$$

where the term $\frac{d\{\varepsilon\}}{d\rho_e}$ shows the dependence of the node potentials $\{\varepsilon\}$ on the variable ρ_e. This dependence is implicit, and we can find an alternative from the system equation. By deriving $\{g\}$, we obtain the term $\frac{d\{\varepsilon\}}{d\rho_e}$ as written:

$$\frac{d\{\varepsilon\}}{d\rho_e} = -\left(\frac{\partial\{g\}}{\partial\{\varepsilon\}}\right)^{-1} \frac{\partial\{g\}}{\partial \rho_e} \tag{25}$$

Rewrite the formula (24) by replacing the term $\frac{d\{\varepsilon\}}{d\rho_e}$ with (25).

$$\frac{dF_x}{d\rho_e} = \frac{\partial F_x}{\partial \rho_e} - \underbrace{\left[\left(\frac{\partial F_x}{\partial\{\varepsilon\}}\right)^T \left(\frac{\partial\{g\}}{\partial\{\varepsilon\}}\right)^{-1}\right]}_{\lambda^T} \frac{\partial\{g\}}{\partial \rho_e} \tag{26}$$

The first term $\frac{\partial F_x}{\partial \rho_e}$ equals zero, because the force calculation region (green in Fig. 1) is outside the design region. The second term $\frac{\partial F_x}{\partial \{\varepsilon\}}$ is related to the objective function, which can be explicitly derived from (22). As depicted in section IIC, the integration path is discretized into segments by a set of elements enveloping the armature (Force region, Fig. 1), and the magnetic field distribution along each segment is approximated by the crossed mesh element, noted as e, using (8). Then, the general expression of elementary force sensitivities with respect to the corresponding node potentials is written as (27). Apply this expression to all the elements in the force region and integrate these sensitivities along the integration path. Finally, we can get the vector $\frac{\partial F_x}{\partial \{\varepsilon\}}$. The third term $\frac{\partial \{g\}}{\partial \{\varepsilon\}}$ is the derivative with respect to the state variables (node potentials). This derivation is known as the Jacobian matrix for a nonlinear system. This Jacobian matrix is the permeance matrix (28), which is updated iteratively in this study. The fourth term $\frac{\partial \{g\}}{\partial \rho_e}$ shows the dependence on each design variable, and it is expressed as (29). Note that the two terms, $\frac{\partial F_x}{\partial \{\varepsilon\}}$ and $\frac{\partial \{g\}}{\partial \{\varepsilon\}}$, depend only on the node potentials $\{\varepsilon\}$, and they are the same for all the design variables. Therefore, it only needs to be computed once.

$$\begin{cases} \dfrac{\partial F_x}{\partial \varepsilon_0^e} = 0 \\ \dfrac{\partial F_x}{\partial \varepsilon_1^e} = \dfrac{1}{2l_x^e} \begin{Bmatrix} -\Lambda_y^e(\varepsilon_1^e - \varepsilon_3^e) \\ +\Lambda_y^e(\varepsilon_4^e - \varepsilon_2^e) \end{Bmatrix} \cdot \begin{Bmatrix} n_x^e \\ n_y^e \end{Bmatrix} \\ \dfrac{\partial F_x}{\partial \varepsilon_2^e} = \dfrac{1}{2l_x^e} \begin{Bmatrix} -\Lambda_x^e(\varepsilon_4^e - \varepsilon_2^e) \\ -\Lambda_y^e(\varepsilon_1^e - \varepsilon_3^e) \end{Bmatrix} \cdot \begin{Bmatrix} n_x^e \\ n_y^e \end{Bmatrix} \\ \dfrac{\partial F_x}{\partial \varepsilon_3^e} = \dfrac{1}{2l_x^e} \begin{Bmatrix} +\Lambda_y^e(\varepsilon_1^e - \varepsilon_3^e) \\ -\Lambda_y^e(\varepsilon_4^e - \varepsilon_2^e) \end{Bmatrix} \cdot \begin{Bmatrix} n_x^e \\ n_y^e \end{Bmatrix} \\ \dfrac{\partial F_x}{\partial \varepsilon_4^e} = \dfrac{1}{2l_x^e} \begin{Bmatrix} +\Lambda_x^e(\varepsilon_4^e - \varepsilon_2^e) \\ +\Lambda_y^e(\varepsilon_1^e - \varepsilon_3^e) \end{Bmatrix} \cdot \begin{Bmatrix} n_x^e \\ n_y^e \end{Bmatrix} \end{cases} \tag{27}$$

$$\frac{\partial \{g\}}{\partial \{\varepsilon\}} = [\Lambda] \tag{28}$$

$$\frac{\partial \{g\}}{\partial \rho_e} = \frac{\partial [\Lambda]}{\partial \rho_e}\{\varepsilon\} - \frac{\partial \{\varphi\}}{\partial \rho_e} \tag{29}$$

where $\frac{d[\Lambda]}{d\rho_e}$ and $\frac{d\{\varphi\}}{d\rho_e}$ are related to the material interpolation scheme (16). The magnetic material nonlinearity is modeled using Norton's method in the design region by a magnetic equivalent circuit. The values of equivalent circuits vary with the operating slope j and material density ρ_e. By deriving (17) and (19), we get a general expression of the equivalent circuit sensitivities:

if $B < B_{sat}$,

$$\begin{cases} \dfrac{d\Lambda_{virt}^{j=1}}{d\rho_e} = n\rho_e^{n-1}(\Lambda_{iron}^{j=1} - \Lambda_{air}) \\ \dfrac{d\varphi_{virt}^{j=1}}{d\rho_e} = 0 \end{cases} \tag{30}$$

else if $B \geq B_{sat}$,

$$\begin{cases} \dfrac{d\Lambda_{virt}^{j=2}}{d\rho_e} = 0 \\ \dfrac{d\varphi_{virt}^{j=2}}{d\rho_e} = \varphi_{sat} \dfrac{n\rho_e^{n-1}(\Lambda_{iron}^{j=1} - \Lambda_{air})\Lambda_{air}}{\Big(\Lambda_{air} + \rho_e^n(\Lambda_{iron}^{j=1} - \Lambda_{air})\Big)^2} \end{cases} \tag{31}$$

Lastly, we assemble these terms in (32) and determine the objective sensitivities.

$$\frac{dF_x}{d\rho_e} = \frac{\partial F_x}{\partial \rho_e} - \lambda^T \left(\frac{d[\Lambda]}{d\rho_e}\{\varepsilon\} - \frac{d\{\varphi\}}{d\rho_e} \right) \tag{32}$$

The FDM can be used to verify the sensitivities by the AVM.

E. Optimization algorithm

Numerous schemes for updating design variables have been proposed in the context of topology optimization problems.

Gradient-based optimization methods, including Sequential Linear Programming (SLP) [25], the Method of Moving Asymptotes (MMA) [26] and the Optimality Criteria (OC) method [20], are highly favored. SLP works by linearizing the objective and constraints based on gradient information. However, one disadvantage is that the linearized problem tends to converge to the corner of the move limits. [27]. MMA is based on convex approximation, but its efficiency depends on asymptote and move limits [28]. The OC updates its design variables based on the optimality condition until convergence is reached. The limitation of the OC method is that it only works by minimizing objective function with a single volume constraint, accompanied by the computational burden associated with determining the Lagrange multiplier. The GOC is an extension of the OC method [27]. Instead of using the bisection method in OC to determine the Lagrange multiplier, the GOC updates its value at every optimization step, and it can have multiple inequality constraints.

By introducing the Lagrange multiplier, the constraint problem (23) could be transferred to an unconstrained Lagrange function (33).

$$\min_{\{\rho_e\}} L(\{\rho_e\}, \gamma) = -F_x(\{\varepsilon\}, \{\rho_e\}) + \gamma\,(c(\{\rho_e\}) + s) \tag{33}$$

where $s \geq 0$ to ensure that the original inequality constraint is satisfied. γ is the introduced Lagrange multiplier. The initial value $\gamma_0 = 1$ is a good starting point, and it is updated iteratively. Among all the several Lagrange multiplier updating methods [29], we choose a simple linear one which has the form:

$$\gamma^{k+1} = \gamma^k(1 + p_0(c^k + \Delta c^k)) \tag{34}$$

where c^k is the constraint at iteration k. If the constraint is violated ($c^k > 0$), the Lagrange multiplier increases, and vice versa. To ensure a smooth change of γ, the effect of change in constraint $\Delta c^k = c^k - c^{k-1}$ is included in the updating algorithm. The p_0 is the update parameter; it has a positive value $p_0 = 1.2$ if both the c and Δc have the same signs, otherwise, $p_0 = 0$ [27]. After updating the Lagrange multiplier, the next step is to update the design variables. A scale factor D_e is defined for each design variable, which has the form:

$$D_e^{k+1} = -\frac{min(0, \frac{dF_x}{d\rho_e}) + \gamma^{k+1} \times min(0, \frac{dc}{d\rho_e})}{max(0, \frac{dF_x}{d\rho_e}) + \gamma^{k+1} \times max(0, \frac{dc}{d\rho_e})} \tag{35}$$

Lastly, the design variables are altered by (36):

$$\rho_e^{k+1} = \rho_e^k \sqrt{D_e^{k+1}} \tag{36}$$

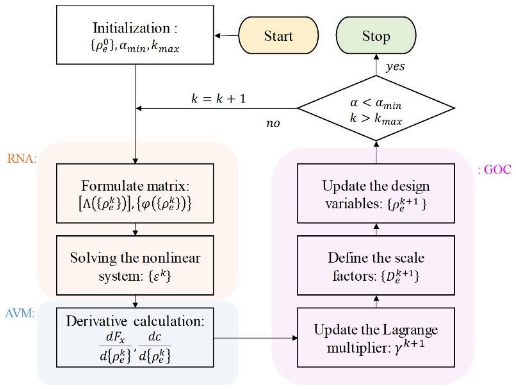

Fig. 12. Flowchart of the topology optimization

TABLE I
THE MAGNETIC ATTRACTIVE FORCE OF THE REFERENCE DESIGN

Modeling	FEA-ref	RNA-ref	RNA-sim	Unit
F_x	195.87	189.28	188.91	N/m

The optimization stops when the step size ($\alpha = \|\Delta\boldsymbol{\rho}\|_2$) is smaller than the minimum step size (e.g. $\alpha_{min} = 1e^{-3}$) or the iteration reaches its maximum value (k_{max}). The flowchart of the optimization algorithm is depicted in Fig. 12.

III. TOPOLOGY OPTIMIZATION

We implemented the topology optimization framework in Matlab R2019b. The electromagnetic actuator under investigation is shown in Fig. 1, together with geometrical dimensions (table II). For a case study, we adopted a mesh configuration outlined in Fig. 1. As indicated in table III, this mesh comprises a total of 864 elements, with 300 elements specifically allocated to the design region. The RNA is applied for parameter and performance evaluation. the material saturation is considered using a simplified two-slope BH curve with knee point B_{sat}. Before conducting the optimization, a critical step is to validate the proposed model. This validation comprises comparing the proposed RNA model against an FEA model. Using the same mesh configuration as seen in Fig.1, we developed three different models: the FEA model with accurate BH curves (FEA-ref), the RNA model with accurate BH curves (RNA-ref), and the RNA model with simplified two-slope BH curves (RNA-sim). We compared their flux density distribution ($|B|$) along two preset lines (L2, L3) shown in Fig. 14, , as well as their magnetic force (F_x). The comparison outcomes are illustrated in Fig. 13, and summarized in table I. Both RNA-ref and RNA-sim can reasonably approximate the flux density distributions observed in FEA-ref, and they exhibit a relative error of approximately 4% regarding the magnetic force. This error would be further minimized with finer mesh resolutions. Compared to RNA-ref, the RNA-sim model enables faster computation with acceptable accuracy. Therefore, given the presented mesh resolution, the RNA model with simplified BH curves seems sufficient in the primary design stage.

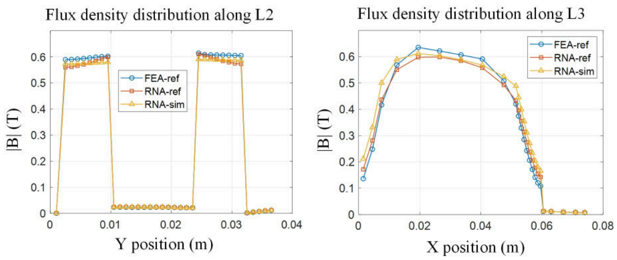

Fig. 13. Validation of the RNA model with the FEA model

TABLE II
SPECIFICATIONS OF THE ELECTROMAGNETIC ACTUATOR

Parameter	Value
Current of coil	1 A
Turns	420
μ_r	26 163 (PowerCore H 105-30)
μ_0	$4\pi \times 10^{-7} H/m$
B$_{sat}$	1.7 T
Length of the simulation domain	75 mm
Width of the simulation domain	37 mm
Depth of the simulation domain	8 mm
Air gap length to the armature	1 mm

TABLE III
MESH PARAMETERS OF THE ELECTROMAGNETIC ACTUATOR

Parameter	Value
Layers in x direction	24
Layers in y direction	36
Mesh elements	864
Mesh elements in the design region	300
Mesh elements in the force region	30
Nodes of mesh	2652

Analyzing the magnetic circuit within the electromagnetic actuator reveals that the material distribution on the right side of the C-core has an important impact on the magnetic force. This area, as indicated in Fig. 14, frequently emphasized in existing literature, was selected as the design region. While a configuration with full material within the design region is certainly not an optimum solution for the optimization, the possibility of minimizing material usage to meet spatial or cost-related requirements is often of considerable interest in TO. Consequently, a volume constraint is introduced into the topology optimization framework. To make a comparison with an existing result, we set the volume fraction constraint to 0.6, aligning with [30].

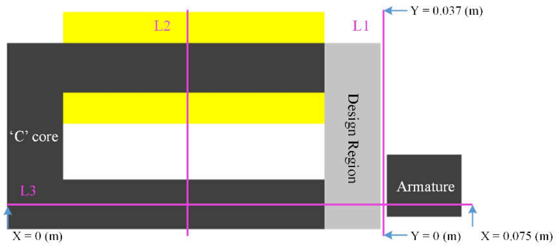

Fig. 14. The design region of the electromagnetic actuator

TABLE IV
PARAMETER SETTING FOR THE OPTIMIZATION

Parameter	Value
Interpolation scheme	SIMP
Penalty coefficient (n)	3
Initial guess (ρ_e^0)	0.3
Low limit (ρ_{min})	$1e^{-3}$
Volume fraction (V_0)	0.6
Minimum step size (α_{min})	$1e^{-3}$
Maximum iterations (k_{max})	100
Update parameter (p_0)	1.2
Force of reference design	195.5 N/m

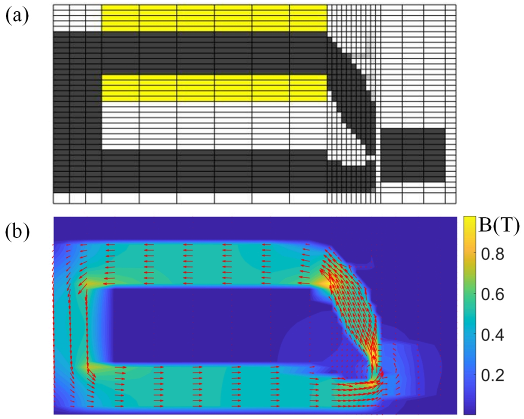

Fig. 15. (a) The optimized topology (254.2 N/m) and (b) its corresponding flux density distribution

The optimization starts from a uniform initial material distribution, and the design variables are updated by the GOC method. A detailed setting for the optimization is listed in the table IV. The optimized topology and its corresponding flux density distribution are depicted in Fig. 15. We presented the parameters history of the first 100 iterations in Fig. 16. The volume fraction constraint is satisfied, and the resultant magnetic force (254.2 N/m) is increased by about 30% compared to the reference design (195.87 N/m).

Comparing the flux density distribution of the reference and optimized design as shown in Fig.17 and Fig.15 (b). We could find that the optimized topology reduces the flux leakage and integrates more flux into the armature, which may illustrate the improvement of the optimized magnetic force. As indicated in Fig. 18, it shows the flux density variation along L1, a line located in the airgap between the ‘C’ core and the armature as shown in Fig. 14.

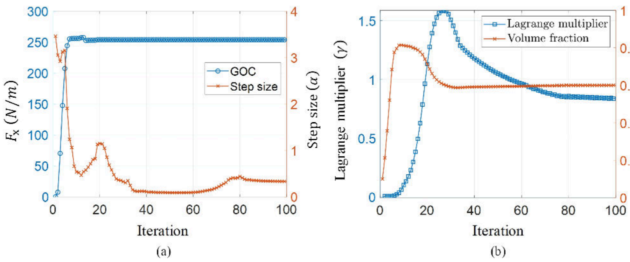

(a) (b)

Fig. 16. The history of the magnetic force, the step size, the Lagrange multiplier, and the volume fraction

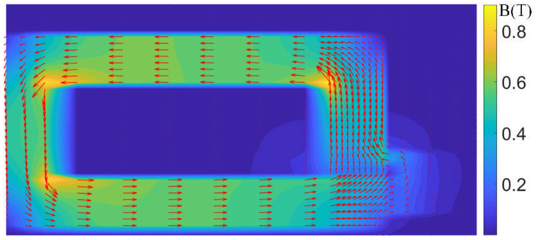

Fig. 17. The flux density distribution of the reference design (Fig.1)

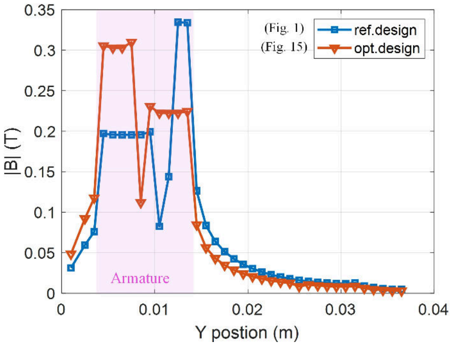

Fig. 18. The flux density variation along L1 (Fig. 14)

Contrary to the OC method, the volume constraint is not satisfied during each iteration with GOC, but by adjusting the Lagrange multiplier γ and satisfying all the required optimality conditions finally, as demonstrated in Fig. 16 (b). The optimization exhibits a slight oscillation around the volume ratio constraint (0.6). This oscillation is also revealed by Fig. 16 (a) which shows the history of the step size. The optimization has a high step size (>1) in the first 8 iterations and then converges slowly. In the last few iterations (83 –100), it keeps a step size of 0.35, which is still far from the minimum constraint ($1e^{-3}$). The optimization terminates when it reaches the maximum number of iterations (100).

A. Impact of initial distribution

To explore the impact of initial points on the final solution, we performed five optimizations with different uniform initial distributions ($\rho_e^0 = 0.1, 0.3, 0.5, 0.7, 0.9$). The optimizations are under the same setting as table IV except for the volume ratio constraint. The optimizations stopped due to reaching the minimum step size (α_{min}), and the results were collected in Fig. 19. From the optimized topologies, we can find that there is no intermediate material, and they vary with each other even though they share the same magnetic force of 253.9 N/m. The optimizations converge to the local optimum.

B. Mesh dependency

To investigate the mesh dependency, we performed three optimizations with different resolutions (138, 300, 912). The

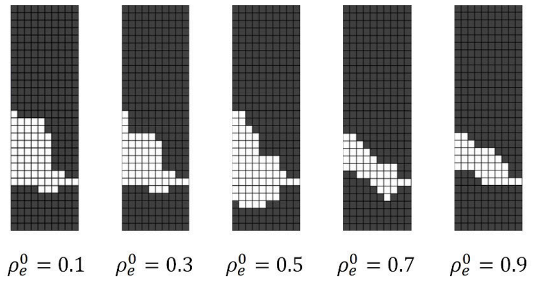

Fig. 19. The optimized topologies (253.9 N/m) with different initial distributions (ρ_0)

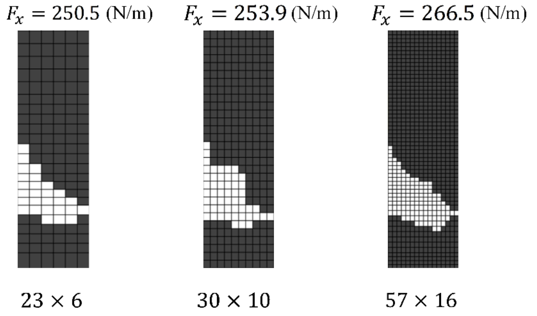

Fig. 20. The optimized topology with different mesh resolutions

optimizations started with a uniform initial distribution ($\rho_e^0 = 0.3$) without any constraint, and the other parameters remained the same in table IV. The results are shown in Fig. 20. We can find that the optimized topologies show similar tendencies but differ from each other in terms of detail. The topology with the finest mesh exhibits the highest magnetic force (266.5 N/m) probably due to the smallest airgap.

C. Density filtering

Sometimes, the optimized topology by the density method may result in grayscale, as indicated in the first optimization result (Fig. 15). To promote clear boundaries, we investigate the application of a density filter in the RNA-based optimization framework. The density filter computes the weighted average of the material densities from neighboring elements within a specified radius r_{min}, as delineated by (37).

$$\tilde{\rho}_e = \frac{1}{\sum_{i \in N_i} H_{ei}} \sum_{i \in N_i} H_{ei} \rho_i \tag{37}$$

where $\tilde{\rho}_e$ is the filtered density of element e, and i is its neighbor element with a total number of N_i. H_{ei} is defined by (38), and Δ is the center distance between two elements (e, i):

$$H_{ei} = \max(0, r_{min} - \Delta(e, i)) \tag{38}$$

The sensitivities with respect to the design variables ρ_e (with N_j neighboring elements) should also be modified by means of the chain rule [20]:

$$\begin{aligned} \frac{dF_x}{d\rho_e} &\rightarrow \sum_{e \in N_j} \frac{1}{\sum_{i \in N_i} H_{ei}} H_{je} \frac{dF_x}{d\tilde{\rho}_e} \\ \frac{dc}{d\rho_e} &\rightarrow \sum_{e \in N_j} \frac{1}{\sum_{i \in N_i} H_{ei}} H_{je} \frac{dc}{d\tilde{\rho}_e} \end{aligned} \tag{39}$$

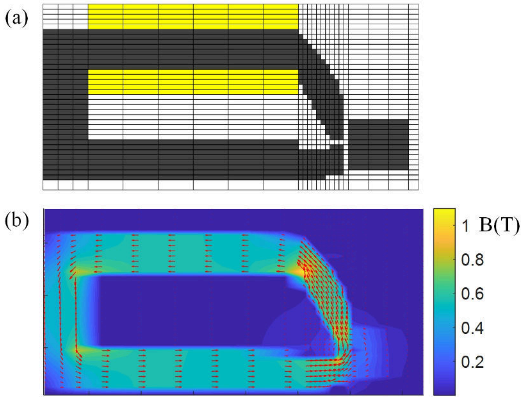

Fig. 21. (a) The optimized topology (255.2 N/m) and (b) its corresponding material density distribution with density filtering

A drawback of density filters is the inevitable grey transition regions between solid and void regions. To overcome this problem, we reduce the filter radius in a continuation approach (e.g. by every 35 iterations) [31].

With the same setting as the first optimization, we include the density filter with a unified filter size of $r_{min} = 1.5$. The optimization result is presented in Fig. 21.

In comparison with Fig. 15, this filtered topology enables a slightly higher magnetic force of 255.2 N/m, and the grayscale is removed, promoting smoother and clearer boundaries between solid and void regions. Moreover, the thin connections are avoided with a density filter, which mitigates the magnetic flux bottleneck problem, as demonstrated in Fig. 15 (b) and Fig. 21 (b). To avoid breaking the magnetic circuit, a mechanical coupling could be introduced into the optimization process.

IV. CONCLUSION

We built a reluctance network model for the electromagnetic actuator, and the material nonlinearity was taken into account. We introduced a simplified BH curve with two slopes to quickly and efficiently consider magnetic saturation in a time-consuming optimization process. A topology optimization based on this modeling framework was successfully implemented for the benchmark problem for the first time. The result presents an improved objective with a satisfied volume ratio constraint. The optimized topology contains few intermediate materials, and the optimization has difficulty obtaining a converged result. This issue can be mitigated by interpolating magnetic reluctivity (ν) instead of magnetic permeability (μ) as suggested in [13] or by introducing filtering and regularization techniques. The initial points highly impact the final solution, and the optimized result is mesh-dependent. The future works involve including the manufacturability and practicality of the optimized designs into the optimization and applying this method to more complex cases, such as magnetic gear.

REFERENCES

[1] M. P. Bendsøe and N. Kikuchi, "Generating optimal topologies in structural design using a homogenization method,"

Computer Methods in Applied Mechanics and Engineering, vol. 71, no. 2, pp. 197–224, Nov. 1988. [Online]. Available: https://linkinghub.elsevier.com/retrieve/pii/0045782588900862

[2] D. Dyck and D. Lowther, "Automated design of magnetic devices by optimizing material distribution," *IEEE Trans. Magn.*, vol. 32, no. 3, pp. 1188–1193, May 1996. [Online]. Available: http://ieeexplore.ieee.org/document/497456/

[3] G. Anagnostou, E. M. Rønquist, and A. T. Patera, "A computational procedure for part design," *Computer Methods in Applied Mechanics and Engineering*, vol. 97, no. 1, pp. 33–48, May 1992. [Online]. Available: https://linkinghub.elsevier.com/retrieve/pii/004578259290106T

[4] H. A. Eschenauer, V. V. Kobelev, and A. Schumacher, "Bubble method for topology and shape optimization of structures," *Structural Optimization*, vol. 8, no. 1, pp. 42–51, Aug. 1994. [Online]. Available: http://link.springer.com/10.1007/BF01742933

[5] G. Allaire, F. Jouve, and A.-M. Toader, "A level-set method for shape optimization," *Comptes Rendus Mathematique*, vol. 334, no. 12, pp. 1125–1130, Jan. 2002. [Online]. Available: https://linkinghub.elsevier.com/retrieve/pii/S1631073X02024123

[6] M. Johnson, M. C. Gardner, and H. A. Toliyat, "A Parameterized Linear Magnetic Equivalent Circuit for Analysis and Design of Radial Flux Magnetic Gears—Part I: Implementation," *IEEE Trans. Energy Convers.*, vol. 33, no. 2, pp. 784–791, Jun. 2018. [Online]. Available: https://ieeexplore.ieee.org/document/8120013/

[7] V. Ostović, *Dynamics of Saturated Electric Machines*. New York, NY: Springer New York, 1989. [Online]. Available: http://link.springer.com/10.1007/978-1-4613-8933-0

[8] H. Diab, S. Asfirane, N. Bracikowski, F. Gillon, and Y. Amara, "Introduction to Mesh Based Generated Lumped Parameter Models for Electromagnetic Problems using Triangular Elements," *Trans. Electr. Mach. Syst.*, vol. 7, no. 1, pp. 21–34, Mar. 2023. [Online]. Available: https://ieeexplore.ieee.org/document/10018857/

[9] G. Watthewaduge and B. Bilgin, "Reluctance Mesh-Based Magnetic Equivalent Circuit Modeling of Switched Reluctance Motors for Static and Dynamic Analysis," *IEEE Trans. Transp. Electrific.*, vol. 8, no. 2, pp. 2164–2176, Jun. 2022. [Online]. Available: https://ieeexplore.ieee.org/document/9638576/

[10] G. Sefkat, "The design optimization of the electromechanical actuator," *Struct Multidisc Optim*, vol. 37, no. 6, pp. 635–644, Feb. 2009. [Online]. Available: http://link.springer.com/10.1007/s00158-008-0254-3

[11] S. L. Ho, S. Yang, and Y. Bai, "A Fast Methodology for Topology Optimizations of Electromagnetic Devices," *IEEE Trans. Magn.*, vol. 53, no. 6, pp. 1–4, Jun. 2017. [Online]. Available: http://ieeexplore.ieee.org/document/7843671/

[12] Y. Okamoto and N. Takahashi, "Investigation of topology optimization of magnetic circuit using density method," *Elect. Eng. Jpn.*, vol. 155, no. 2, pp. 53–63, Apr. 2006. [Online]. Available: https://onlinelibrary.wiley.com/doi/10.1002/eej.20259

[13] J. S. Choi and J. Yoo, "Structural optimization of ferromagnetic materials based on the magnetic reluctivity for magnetic field problems," *Computer Methods in Applied Mechanics and Engineering*, vol. 197, no. 49-50, pp. 4193–4206, Sep. 2008. [Online]. Available: https://linkinghub.elsevier.com/retrieve/pii/S0045782508001771

[14] Jae Seok Choi and Jeonghoon Yoo, "Structural Topology Optimization of Magnetic Actuators Using Genetic Algorithms and ON/OFF Sensitivity," *IEEE Trans. Magn.*, vol. 45, no. 5, pp. 2276–2279, May 2009. [Online]. Available: http://ieeexplore.ieee.org/document/4816002/

[15] S. Yang, S. Asfirane, S. Hlioui, S. Mezani, G. Krebs, Y. Amara, G. Barakat, M. Gabsi, and W. Hua, "Introduction to mesh based generated lumped parameter models for electromagnetic problems," *Trans. Electr. Mach. Syst.*, vol. 5, no. 2, pp. 152–162, Jun. 2021. [Online]. Available: https://ieeexplore.ieee.org/document/9473194/

[16] D. Ceylan, R. Zeinali, B. Daniels, K. O. Boynov, and E. A. Lomonova, "A Novel Modeling Technique via Coupled Magnetic Equivalent Circuit With Vector Hysteresis Characteristics of Laminated Steels," *IEEE Trans. on Ind. Applicat.*, vol. 59, no. 2, pp. 1481–1491, Mar. 2023. [Online]. Available: https://ieeexplore.ieee.org/document/9933897/

[17] M.-F. Hsieh and Y.-C. Hsu, "A generalized magnetic circuit modeling approach for design of surface permanent-magnet machines," *IEEE Transactions on Industrial Electronics*, vol. 59, no. 2, pp. 779–792, 2011.

[18] M. Stolpe and K. Svanberg, "An alternative interpolation scheme for minimum compliance topology optimization," *Struct Multidisc Optim*, vol. 22, no. 2, pp. 116–124, Sep. 2001. [Online]. Available: http://link.springer.com/10.1007/s001580100129

[19] D. Lukáš, "An Integration of Optimal Topology and Shape Design for Magnetostatics," in *Scientific Computing in Electrical Engineering*, H.-G. Bock, F. De Hoog, A. Friedman, A. Gupta, H. Neunzert, W. R. Pulleyblank, T. Rusten, F. Santosa, A.-K. Tornberg, A. M. Anile, G. Alì, and G. Mascali, Eds. Berlin, Heidelberg: Springer Berlin Heidelberg, 2006, vol. 9, pp. 227–232, series Title: Mathematics in Industry. [Online]. Available: http://link.springer.com/10.1007/978-3-540-32862-9-32

[20] E. Andreassen, A. Clausen, M. Schevenels, B. S. Lazarov, and O. Sigmund, "Efficient topology optimization in MATLAB using 88 lines of code," *Struct Multidisc Optim*, vol. 43, no. 1, pp. 1–16, Jan. 2011. [Online]. Available: http://link.springer.com/10.1007/s00158-010-0594-7

[21] J. D. Deaton and R. V. Grandhi, "A survey of structural and multidisciplinary continuum topology optimization: post 2000," *Struct Multidisc Optim*, vol. 49, no. 1, pp. 1–38, Jan. 2014. [Online]. Available: http://link.springer.com/10.1007/s00158-013-0956-z

[22] S. Sanogo and F. Messine, "Topology optimization in electromagnetism using SIMP method: Issues of material interpolation schemes," *COMPEL*, vol. 37, no. 6, pp. 2138–2157, Nov. 2018. [Online]. Available: https://www.emerald.com/insight/content/doi/10.1108/COMPEL-04-2017-0170/full/html

[23] A. Benhama, A. Williamson, and A. Reece, "Force and torque computation from 2-D and 3-D finite element field solutions," *IEE Proc., Electr. Power Appl.*, vol. 146, no. 1, p. 25, 1999. [Online]. Available: https://digital-library.theiet.org/content/journals/10.1049/ip-epa-19990219

[24] R. El Bechari, F. Guyomarch, and S. Brisset, "The Adjoint Variable Method for Computational Electromagnetics," *Mathematics*, vol. 10, no. 6, p. 885, Mar. 2022. [Online]. Available: https://www.mdpi.com/2227-7390/10/6/885

[25] J. S. Choi and J. Yoo, "Simultaneous structural topology optimization of electromagnetic sources and ferromagnetic materials," *Computer Methods in Applied Mechanics and Engineering*, vol. 198, no. 27-29, pp. 2111–2121, May 2009. [Online]. Available: https://linkinghub.elsevier.com/retrieve/pii/S0045782509000863

[26] K. Svanberg, "The method of moving asymptotes—a new method for structural optimization," *Numerical Meth Engineering*, vol. 24, no. 2, pp. 359–373, Feb. 1987. [Online]. Available: https://onlinelibrary.wiley.com/doi/10.1002/nme.1620240207

[27] N. H. Kim, T. Dong, D. Weinberg, and J. Dalidd, "Generalized Optimality Criteria Method for Topology Optimization," *Applied Sciences*, vol. 11, no. 7, p. 3175, Apr. 2021. [Online]. Available: https://www.mdpi.com/2076-3417/11/7/3175

[28] T. Jiang *et al.*, "A first order method of moving asymptotes for structural optimization," *WIT Transactions on the Built Environment*, vol. 14, 1970.

[29] S. N. Patnaik, J. D. Guptill, and L. Berke, "Merits and limitations of optimality criteria method for structural optimization," *Numerical Meth Engineering*, vol. 38, no. 18, pp. 3087–3120, Sep. 1995. [Online]. Available: https://onlinelibrary.wiley.com/doi/10.1002/nme.1620381806

[30] F. Lucchini, R. Torchio, V. Cirimele, P. Alotto, and P. Bettini, "Topology optimization for electromagnetics: A survey," *IEEE Access*, vol. 10, pp. 98 593–98 611, 2022.

[31] O. Sigmund and K. Maute, "Topology optimization approaches: A comparative review," *Struct Multidisc Optim*, vol. 48, no. 6, pp. 1031–1055, Dec. 2013. [Online]. Available: http://link.springer.com/10.1007/s00158-013-0978-6